New type of the interface evolution in the Richtmyer-Meshkov instability

By S. I. Abarzhi and M. Herrmann

1. Motivation and objectives

When a shock wave passes an interface between two fluids with different values of the acoustic impedance, the misalignment of the pressure and density gradients results in a growth of the interface perturbations and causes the development of the Richtmyer-Meshkov instability (RMI) (Richtmyer 1960; Meshkov 1969). The instability produces with time the turbulent mixing of the fluids, which controls many physical and technological processes, such as inertial confinement fusion, supernova explosion, and impact dynamics of liquids (Kull 1991). Reliable description of the turbulent mixing is the basic objective of studies of RMI (Kull 1991; Schneider *et al.* 1998).

Observations report the following evolution of the Richtmyer-Meshkov instability. In the linear regime, the light fluid accelerates impulsively the heavy fluid, and a small amplitude perturbation of the fluid interface grows linearly with time (Richtmyer 1960; Meshkov 1969). The acceleration value is determined by the shock-interface interaction, which is essentially non-local and results in a baroclinic production of vorticity (Haan 1991; Velikovich & Dimonte 1996; Vandenboomgaerde *et al.* 1998; Wouchuk 2001). In the non-linear regime, a structure of bubbles and spikes appear (Pavlenko *et al.* 2000; Chebotareva *et al.* 1999; Jacobs & Sheeley 1996; Bonazza & Sturtevant 1996). The light (heavy) fluid penetrates the heavy (light) fluid in bubbles (spikes). The bubbles decelerate and the spikes move steadily. Small-scale structures appear on the side of evolving spikes due to shear, and the direct cascade of the fluid energy may occur (Matsuoka *et al.* 2003). For a finite-amplitude perturbation, the fluid energy may be transferred also to larger scales (Alon *et al.* 1995; Oron *et al.* 2001). Eventually, a mixing zone develops. In the chaotic regime, the bubbles and spikes decelerate, and their positions are described by power-law time-dependencies with exponents determined by the density ratio (Schneider *et al.* 1998; Dimonte 2000).

The dynamics of the Richtmyer-Meshkov instability is far from being completely understood. For a long time, the theoretical models and numerical simulations failed to predict the growth-rate in the linear RMI observed in experiments (Holmes *et al.* 1999). Only recently, a rigorous theory has accounted for the non-local character of the interface dynamics in the case of strong and weak shocks and provided therefore for impulsive models the correct value of the acceleration (Wouchuk 2001). To describe the nonlinear RMI, several models have applied a single-mode approximation, which presumed locality of the bubble (spike) dynamics (Alon *et al.* 1995; Goncharov 2002). Some other models have used an empiric equation with adjustable parameters to balance "drag" and "inertia" in the flow (Oron *et al.* 2001; Dimonte 2000). All these models however cannot explain the observations and remain subjects for controversy (Dimonte 2000). There is a strong need in a formal theoretical approach and in experiments and simulations with systematic variation of parameters and improved diagnostics. In this work we suggest analytical and numerical solutions describing the nonlinear coherent dynamics

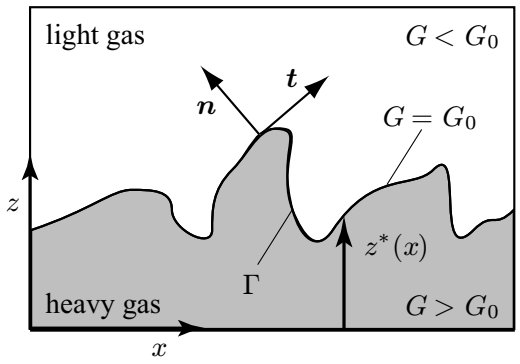

FIGURE 1. Interface definition.

of two-dimensional Richtmyer-Meshkov instability for fluids with a finite density ratio. Our results predict new properties of the nonlinear evolution of RMI, explain existing experiments, and identify new sensitive diagnostic parameters.

2. Governing equations

The dynamics of the Richtmyer-Meshkov instability are governed by a system of conservation laws, which are compressible two-dimensional Navier-Stokes with the initial conditions and the boundary conditions at the fluid interface,

$$\frac{\partial \rho}{\partial t} + \nabla \cdot (\rho \boldsymbol{v}) = 0 \tag{2.1}$$

$$\frac{\partial \rho \boldsymbol{v}}{\partial t} + \nabla \cdot (\rho \boldsymbol{v}\boldsymbol{v}) + \nabla p + \nabla \cdot \overline{\overline{\tau}} = 0 \tag{2.2}$$

$$\frac{\partial \rho E}{\partial t} + \nabla \cdot ([\rho E + p]\, \boldsymbol{v}) + \nabla \cdot \boldsymbol{q} + \overline{\overline{\tau}} : \nabla \boldsymbol{v} = 0\,. \tag{2.3}$$

Here, ρ denotes the density, $\boldsymbol{v}$ the velocity vector, p the pressure, $\overline{\overline{\tau}}$ the stress tensor, E the total energy, and $\boldsymbol{q}$ the heat flux vector. All quantities are either in the heavy gas, denoted by the subscript h in the following, or in the light gas, denoted by the subscript l. The above system of equations is closed by the ideal gas law,

$$p = \rho \Phi T\,, \tag{2.4}$$

with Φ the gas constant and T the temperature.

The interface Γ located at $z^*(x,t)$ separating heavy from light gas, is described by a level set scalar G, see Fig. 1. Defining

$$G(\boldsymbol{x},t)\Big|_\Gamma = G_0 = \text{const}\,, \tag{2.5}$$

with $G(\boldsymbol{x},t) < G_0$ in the light gas and $G(\boldsymbol{x},t) > G_0$ in the heavy gas, compare Fig. 1, an evolution equation for the scalar G can be derived by simply differentiating Eq. (2.5) with respect to time,

$$\frac{\partial G}{\partial t} + \boldsymbol{v} \cdot \nabla G = 0\,. \tag{2.6}$$

This equation is called the level set equation (Osher & Sethian 1988). It is easy to see that Eq. (2.6) is independent of the choice of G away from the interface. However, to

facilitate the numerical solution of Eq. (2.6), G is chosen to be a distance function away from the interface,

$$|\nabla G|\Big|_{G\neq G_0} = 1\,. \tag{2.7}$$

Using the level set scalar, geometrical properties of the interface, like its normal vector $\boldsymbol{n}$ or curvature ζ, can be easily calculated,

$$\boldsymbol{n} = \frac{\nabla G}{|\nabla G|}\,, \qquad \kappa = \nabla\cdot\boldsymbol{n}\,. \tag{2.8}$$

There is no mass flow across the moving interface, and the normal component of velocity, pressure and temperature are continuous at the fluid interface:

$$\boldsymbol{v}_{n,h}\big|_\Gamma = \boldsymbol{v}_{n,l}\big|_\Gamma \tag{2.9}$$

$$\boldsymbol{v}_{t,h}\big|_\Gamma = \boldsymbol{v}_{t,l}\big|_\Gamma \tag{2.10}$$

$$p_h\big|_\Gamma = p_l\big|_\Gamma \tag{2.11}$$

$$T_h\big|_\Gamma = T_l\big|_\Gamma\,. \tag{2.12}$$

The flow has no mass sources, and the boundary conditions at the infinity close the set of the governing equations

$$\boldsymbol{v}_h\big|_{z=+\infty} = \boldsymbol{v}_l\big|_{z=-\infty} = 0\,. \tag{2.13}$$

Initially, the fluid interface is slightly disturbed with a small amplitude co-sinusoidal perturbation, $z^*(x, t=0) \sim (1/k)\cos(kx)$, where $k = 2\pi/\lambda$ is the wave-vector, and λ is the spatial period in the x-direction. The perturbation should be symmetric, in order a stable coherent structure of the bubbles and spikes to occur. The density ratio or the Atwood number $A = (\rho_h - \rho_l)/(\rho_h + \rho_l)$ is a determining factor of RMI dynamics.

3. Non-local theoretical solutions

Based on the observations, we divide the fluid interface into active regions (small scales) with intensive vorticity, and passive regions (large scales) which are simply advected. If the energy cascades are not extensive (i.e., the fluid densities are not very similar, the perturbation amplitude is small, and the initial shock is weak), then, a considerable part of the fluid energy concentrates in the large-scale coherent motion with $\nabla\cdot\boldsymbol{v}_{h(l)} = 0$ and $\nabla\times\boldsymbol{v}_{h(l)} = 0$. To find the nonlinear solutions, describing the dynamics of the bubble front in a vicinity of its tip, we reduce the Eqs. (2.1), (2.2), (2.9), and (2.11) to a local dynamical system. All calculations are performed in the frame of reference moving with velocity $v(t)$ in the z-direction, where $v(t)$ is the velocity at the bubble tip in the laboratory frame of reference. For the large-scale motion $\boldsymbol{v}_{h(l)} = \nabla\Phi_{h(l)}$, and we expand the potential $\Phi_{h(l)}$ as a Fourier series,

$$\Phi_h = \sum_{m=1}^{\infty} \Phi_m(t)\big(\cos(mkx)\exp(-mkz)/mk + z\big) \tag{3.1}$$

$$\Phi_l = \sum_{m=1}^{\infty} \tilde{\Phi}_m(t)\big(\cos(mkx)\exp(mkz)/m - z\big) \tag{3.2}$$

For $x \approx 0$ the interface has the form $z^* = \sum_{N=1}^{\infty}\zeta_N(t)x^{2N}$, where $\zeta_1(t) < 1$ is the

principal curvature at the bubble tip, and N is the order of approximation. Substituting these expressions in the governing equations, taking the first integral of Eq. (2.2), and re-expanding Eqs. (2.9) and (2.11) for $x \approx 0$, we derive a system of ordinary differential equations for the surface variables $\zeta_N(t)$, and the moments $M_n(t) = \sum_{m=1}^{\infty} \Phi_m(t)(km)^n$ and $\tilde{M}_n(t) = \sum_{m=1}^{\infty} \tilde{\Phi}_m(t)(km)^n$ where n is integer. For $N = 1$, one has from Eqs. (2.9)-(2.13) respectively

$$\dot{\zeta}_1 = 3\zeta_1 M_1 + M_2/2 = 3\zeta_1 \tilde{M}_1 - \tilde{M}_2/2, \tag{3.3}$$

$$\big(\dot{M}_1/2 + \zeta_1 \dot{M}_0 - M_1^2/2 - \zeta_1\big)\rho_h = \big(\dot{\tilde{M}}_1/2 - \zeta_1 \dot{\tilde{M}}_0 - \tilde{M}_1^2/2 - \zeta_1\big)\rho_l, \tag{3.4}$$

$$M_0(t) = -\tilde{M}_0(t) = -v(t)\,. \tag{3.5}$$

The system (3.3)-(3.5) describes the local dynamics of the bubble as long as the period of the structure is invariable, and the energy cascades are not extensive. The presentation in terms of moments allows one to account for the effect of higher-order correlations. The time-scale in Eqs. (3.3)-(3.5) is $\tau = 1/kv_0$, where v_0 is the absolute value of the initial velocity. For $t/\tau \ll 1$, the dynamical system (3.3)-(3.5) has regular asymptotic solutions with time independent surface variables ζ_N and with velocity v and moments M_n, $\tilde{M}_n$ decaying as $1/t$.

It is easy to see that the local system (3.3)-(3.5) cannot be satisfied in a single-mode approximation. One may derive, for example, a single-mode solution of the Layzer-type, which conserve mass, momentum and has no mass sources. For this bubble $\zeta_1 = \zeta_L = -Ak/6$ and velocity $v = v_L = (1 - A^2/3)/Ak$, however the solution does not satisfy Eqs. (2.9) and (3.3) and requires mass flux across the interface. To reproduce the parameters of the drag model (Oron *et al.* 2001) with $\zeta_1 = \zeta_D = -k/6$ and $v = v_D = (1 + A/3)/k(1 + A)$, one should violate Eqs. (2.13) and (3.5) and introduce a source of mass of the light fluid (Goncharov 2002). Obviously, these solutions are unphysical, because they violate the conservation laws.

To obtain regular asymptotic solutions describing the nonlinear dynamics of the bubble front, one should account for the non-local properties of the flow that has singularities. The singularities determine the interplay of harmonics in the global flow and the local dynamical system, and affect therefore the shape of the regular bubble. We find a continuous family of regular asymptotic solutions for Eqs. (3.3)-(3.5), parameterized by the principal curvature at the bubble tip, and choose the fastest solution in the family as the physically significant one. For $N = 1$ the bubble velocity as the function of the bubble curvature is

$$v = \frac{3}{2kt}\frac{\big(1 + A(\zeta_1/k) - 12A(\zeta_1/k)^3\big)}{\big(A - 4(\zeta_1/k) + 4A(\zeta_1/k)^2\big)}\big(1 - 4(\zeta_1/k)^2\big), \tag{3.6}$$

where $\zeta_{cr} < \zeta < 0$. For the family solutions (3.6), the interplay of harmonics is well captured, the higher order corrections for the velocity and lowest-order amplitudes are small, the solutions converge, yet, most of them are unstable. The fastest stable solution in the family (3.6) is the solution with

$$\zeta_1 = \zeta_A, = 0 \quad v = v_A = 3/2Akt \tag{3.7}$$

The foregoing theoretical results suggest the following evolution of the bubble front in the Richtmyer-Meshkov instability. In the linear regime of RMI, the bubble curvature and velocity change as $\sim t$; in the weakly non-linear regime, the curvature reaches an extreme value, dependent on the initial conditions and the Atwood number; asymptotically, the

bubble flattens and decelerates. For $A < 1$ the bubbles move faster than those for $A = 1$, and for all A the bubbles flatten asymptotically. The flattening of the bubble front is a distinct feature of RMI universal for all A. It follows from the fact that RM bubbles decelerate. As $A \sim 0$, the velocity $v \sim \infty$ and this suggests that for fluids with similar densities the bubble velocity has a much faster time-dependence, such as t^a where $-1 < a < 0$, in a qualitative agreement with experiments of Jacobs & Sheeley (1996), where for $A \sim 0$ the dependence $1/t$ was shown to underestimate the velocity data.

4. Numerical method

In our numerical simulations, the Navier-Stokes equations (2.1)-(2.3) are solved using a hybrid capturing-tracking scheme, originally proposed by Smiljanovski *et al.* (1997) for deflagration waves. When applying this scheme to the RMI, its key idea is to explicitly track the location and motion of the interface between the light and the heavy gas by the level set equation (2.6), whereas all other fluid phenomena like shocks and expansion fans are captured. The main advantage of this approach is that while the simplicity and robustness of standard capturing schemes can be retained, the interfacial processes are described with accuracy comparable to standard tracking schemes. In the following two sections, the hybrid capturing-tracking scheme is summarized briefly. The interested reader is referred to Smiljanovski *et al.* (1997) for a more detailed description.

4.1. *In-cell-reconstruction*

In finite volume schemes, the cell value of a conserved quantity $\boldsymbol{U}^{i,j}$ is defined as the volume average of that quantity,

$$\boldsymbol{U}^{i,j} = \frac{1}{V^{i,j}} \int_{V^{i,j}} \boldsymbol{U}(\boldsymbol{x}')d\boldsymbol{x}' \,, \tag{4.1}$$

averaged over the cell volume $V^{i,j}$. Assuming piecewise constant distributions of $\boldsymbol{U}$ for each fluid within each cell, Eq. (4.1) reduces to

$$\boldsymbol{U}^{i,j} = \alpha \boldsymbol{U}_h^{i,j} + (1-\alpha)\boldsymbol{U}_l^{i,j} \,, \tag{4.2}$$

where α is the heavy gas cell volume fraction that can easily be calculated from the level set scalar G,

$$\alpha = \frac{1}{V^{i,j}} \int_{V^{i,j}} H(G(\boldsymbol{x}') - G_0)d\boldsymbol{x}' \,, \tag{4.3}$$

with H the Heavyside function.

The key idea of the in-cell-reconstruction scheme is to reconstruct both $\boldsymbol{U}_h^{i,j}$ and $\boldsymbol{U}_l^{i,j}$ from $\boldsymbol{U}^{i,j}$, see Fig. 2, and to use only the reconstructed two states to calculate cell face fluxes in cells containing part of the interface. Combining the jump conditions of $\boldsymbol{U}$ across the interface, Eqs. (2.9) - (2.12), with (4.2) and Eqs. (4.3), the cell values $\boldsymbol{U}_h^{i,j}$ and $\boldsymbol{U}_l^{i,j}$ in each cell containing part of the interface can be reconstructed from $\boldsymbol{U}^{i,j}$.

4.2. *Cell update*

The numerical solution is evolved in time using an operator splitting technique (Strang 1967),

$$\boldsymbol{U}^{n+1} = \mathcal{C}^x_{\Delta t/2}\mathcal{C}^z_{\Delta t/2}\mathcal{D}_{\Delta t}\mathcal{C}^z_{\Delta t/2}\mathcal{C}^x_{\Delta t/2}\,\boldsymbol{U}^n \,, \tag{4.4}$$

where $\mathcal{C}$ denotes the convection operator, $\mathcal{D}$ the diffusion operator, $\boldsymbol{U}^n$ the cell volume averaged solution at time t^n, and $\boldsymbol{U}^{n+1}$ the cell volume averaged solution at $t^{n+1} =$

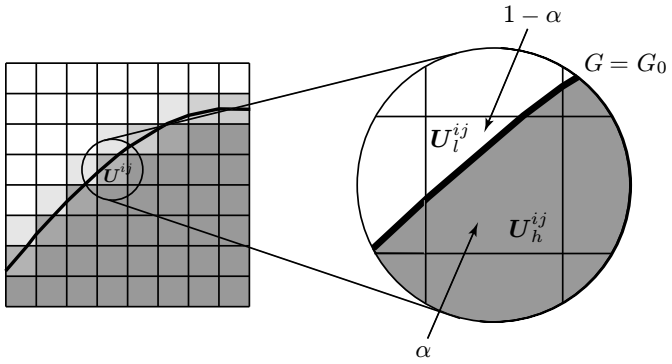

FIGURE 2. In-cell-reconstruction.

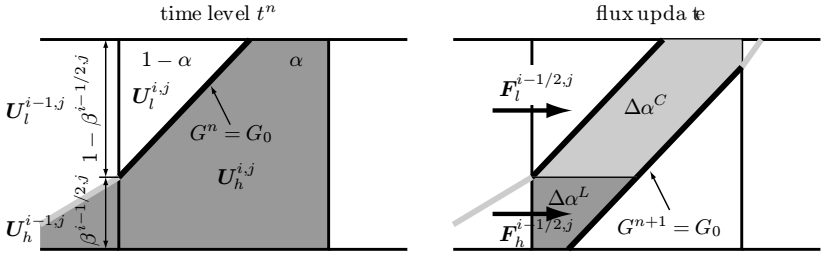

FIGURE 3. Flux update in cells containing part of the interface.

$t^n + \Delta t$. In order to calculate the correct update, all gradients in the individual operator steps must be calculated using only cell values of the same fluid type.

In the diffusion operator $\mathcal{D}$, we calculate all gradients using 2nd order central differences. The corresponding stencils across the interface thus involve the reconstructed cell values $\boldsymbol{U}_h$ respectively $\boldsymbol{U}_l$ plus one additional adjacent cell value on the opposite side of the interface. This cell has to be first transformed into the corresponding matching state using Eqs. (2.9)-(2.12) before the gradients are evaluated. In this operation, our method resembles the ghost fluid approach (Fedkiw *et al.* 1999).

Since the convection operator $\mathcal{C}$ is split into each spatial direction, we will only focus on the x-direction operator in the following. If a cell (i, j) and its directly adjacent neighbors do not contain part of the interface, $\boldsymbol{U}^{n,i,j}$ is advanced in time by

$$\boldsymbol{U}^{n+1,i,j} = \boldsymbol{U}^{n,i,j} + \frac{\Delta t}{\Delta x}\left(\boldsymbol{F}^{i-1/2,j} - \boldsymbol{F}^{i+1/2,j}\right) . \tag{4.5}$$

In our numerical method we solve cell face Riemann problems using a 2nd order wave distribution algorithm due to LeVeque (1990) and formally recast the individual wave contributions in the form of cell face fluxes $\boldsymbol{F}^{i-1/2,j}$ and $\boldsymbol{F}^{i+1/2,j}$. However, special care must be taken, if (i, j) contains part of the interface at t^n or t^{n+1}, as shown in Fig. 3.

To ensure the correct flux calculation, individual cell face fluxes for both the heavy and the light gas must be calculated using only (reconstructed) quantities of the respective fluid,

$$\boldsymbol{F}_h^{i-1/2,j} = \boldsymbol{F}_h^{i-1/2,j}\left(\boldsymbol{U}_{h-}^{i-1/2,j}, \boldsymbol{U}_{h+}^{i-1/2,j}\right) \tag{4.6}$$

$$\boldsymbol{F}_l^{i-1/2,j} = \boldsymbol{F}_l^{i-1/2,j}\left(\boldsymbol{U}_{l-}^{i-1/2,j}, \boldsymbol{U}_{l+}^{i-1/2,j}\right) . \tag{4.7}$$

Here, the subscripts $-$ and $+$ denote the left-hand side respectively right-hand side approximation of $\boldsymbol{U}_{h,l}^{i-1/2,j}$. Then, the average cell face flux $\boldsymbol{F}^{i-1/2,j}$ is

$$\boldsymbol{F}^{i-1/2,j} = \beta^{i-1/2,j}\boldsymbol{F}_h^{i-1/2,j} + (1-\beta^{i-1/2,j})\boldsymbol{F}_l^{i-1/2,j}\,, \tag{4.8}$$

with β the heavy gas cell face fraction, see Fig. 3. Note that because our convection operator is based upon a wave distribution scheme, $\boldsymbol{F}^{i-1/2,j}$ only takes those wave contributions into account that arise from the cell face Riemann problem. Since the interface itself constitutes a separate wave, its contribution to the change of $\boldsymbol{U}^{i,j}$ has to be taken into account additionally,

$$\begin{aligned}\Delta\boldsymbol{U}^{i,j} = {} & \Delta\alpha^C\left(\boldsymbol{U}_h^{i,j} - \boldsymbol{U}_l^{i,j}\right) + \\ & \Delta\alpha^L\left(\boldsymbol{U}_h^{i-1,j} - \boldsymbol{U}_l^{i-1,j}\right) + \Delta\alpha^R\left(\boldsymbol{U}_h^{i+1,j} - \boldsymbol{U}_l^{i+1,j}\right)\,.\end{aligned} \tag{4.9}$$

Here, $\Delta\alpha^C$ is the change of the heavy gas cell volume fraction due to the movement of the interface within the cell (i,j) itself, and $\Delta\alpha^L$ and $\Delta\alpha^R$ are the contributions due to movement from adjacent cells to the left respectively right, see Fig. 3. Note that Eq. (4.9) implies that the global conservation property of the numerical scheme is now dependent on the accuracy with which the individual $\Delta\alpha$ are calculated and hence relies on the accuracy of the level set method.

Finally, combining Eq. (4.8) and Eq. (4.9) yields the update for $\boldsymbol{U}^{i,j}$ in cells that contain part of the interface

$$\begin{aligned}\boldsymbol{U}^{n+1,i,j} = \boldsymbol{U}^{n,i,j} + \frac{\Delta t}{\Delta x}\ & \Big\{\left(\beta^{i-1/2,j}\boldsymbol{F}_h^{i-1/2,j} + (1-\beta^{i-1/2,j})\boldsymbol{F}_l^{i-1/2,j}\right) - \\ & \left(\beta^{i+1/2,j}\boldsymbol{F}_h^{i+1/2,j} + (1-\beta^{i+1/2,j})\boldsymbol{F}_l^{i+1/2,j}\right) + \\ & \Delta\alpha^C\left(\boldsymbol{U}_h^{i,j} - \boldsymbol{U}_l^{i,j}\right) + \Delta\alpha^L\left(\boldsymbol{U}_h^{i-1,j} - \boldsymbol{U}_l^{i-1,j}\right) + \\ & \Delta\alpha^R\left(\boldsymbol{U}_h^{i+1,j} - \boldsymbol{U}_l^{i+1,j}\right)\Big\}\end{aligned} \tag{4.10}$$

One of the major advantages of using Eq. (4.10) is the fact that the CFL-condition can be based on the grid size Δx of the underlying grid, because cell updates are performed only on the cell volume averaged quantities.

5. Results

We present the numerical results of the RMI calculated for a shock Mach number of Ma = 1.2 and two different Atwood and Reynolds numbers. The fist case corresponds to the SF_6/Air experiment of Benjamin *et al.* (1993) with $A = 0.67$ and Re = 11442, whereas in the second case $A = 0.9$ and Re = 6977. The Reynolds numbers are calculated using the bubble velocity V in the laboratory frame of reference and the wave length λ. The initial interface of wave length $\lambda = 0.0375\,\mathrm{m}$ and amplitude $a_0 = 0.0024\,\mathrm{m}$ is located at $z = 0\,\mathrm{m}$. All simulations are performed in a $[-1.1\,\mathrm{m}, 0.3\,\mathrm{m}] \times [-0.01875\,\mathrm{m}, 0.01875\,\mathrm{m}]$ box resolved by 2352×63 equidistant cartesian grid cells.

Figure 4 depicts the temporal evolution of the interface shape for $A = 0.67$, whereas Fig. 5 shows the interface shapes for $A = 0.9$. In both cases, a spike of heavy gas is formed that penetrates ever further into the light gas. In the $A = 0.67$ case, the spike takes on the typical mushroom-like shape, whereas in the $A = 0.9$ the spike simply bulges

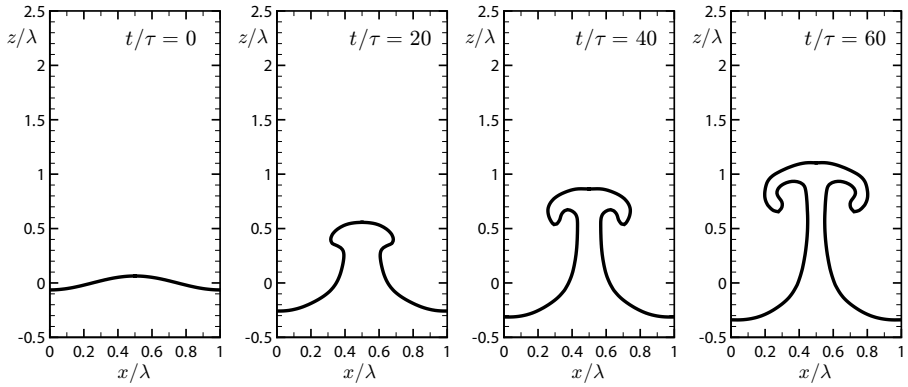

FIGURE 4. Temporal evolution of the interface for A=0.67.

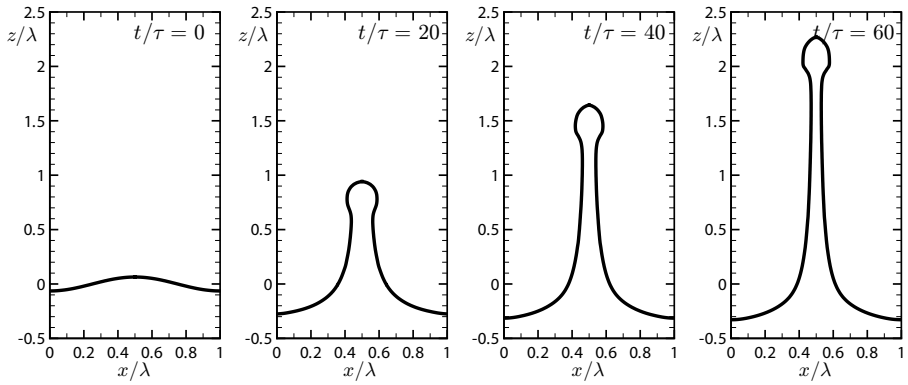

FIGURE 5. Temporal evolution of the interface for A=0.9.

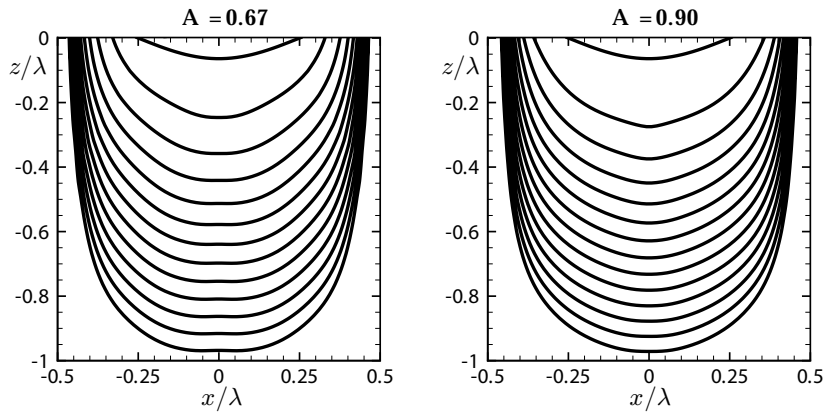

FIGURE 6. Shape of the bubble front for A=0.67 (left) and A=0.9 (right) plotted every $\Delta t/\tau = 10$. Each interface is shifted by $\Delta z = -0.05$.

at the end. This difference is most likely due to the employed numerical resolution that is not sufficient to resolve the apparently smaller scale spike mushroom structure in the $A = 0.9$ case.

Figure 6 shows the temporal evolution of the bubble front for both cases. The flattening

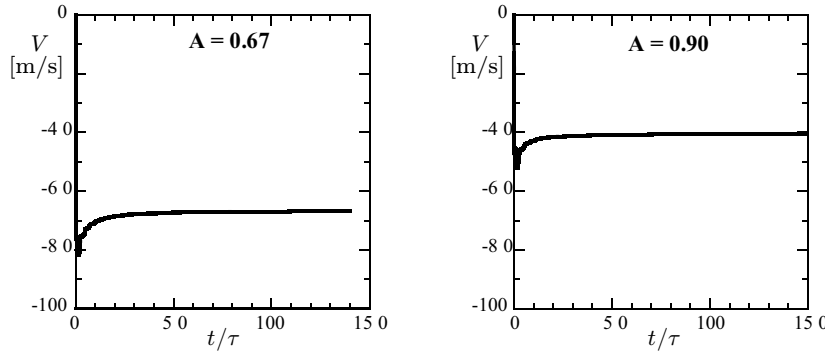

FIGURE 7. Bubble velocity V in the laboratory frame of reference for $A = 0.67$ (left) and $A = 0.9$ (right).

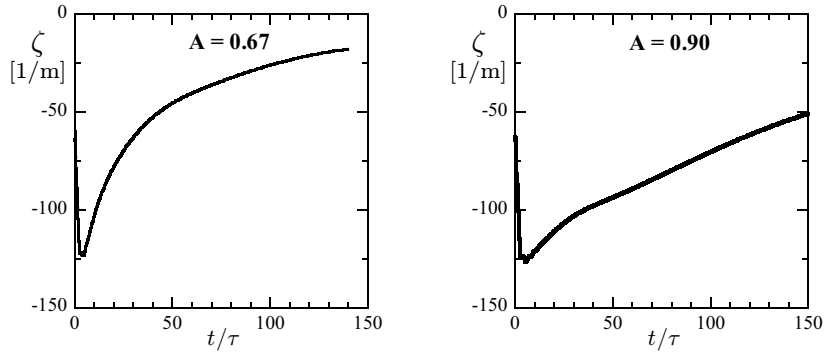

FIGURE 8. Bubble curvature ζ for $A = 0.67$ (left) and $A = 0.9$ (right).

of the bubble front that is predicted by non-local theory is clearly visible in both cases, but is more pronounced in the $A = 0.67$ case. Also, the $A = 0.67$ case exhibits some tiny oscillations of the bubble front at later times that are not visible in the $A = 0.9$ case.

The bubble velocity V in the laboratory frame of reference is depicted in Fig. 7. Initially being at rest, both bubbles are impulsively accelerated by the passing shock. As predicted by non-local theoretical analysis, the bubble velocity reaches a local maximum in the weakly non-linear regime and then asymptotically decelerates to a constant velocity. In the laboratory frame of reference the asymptotic bubble velocity is $V = 66.8$ m/s for $A = 0.67$ and $V = 40.7$ m/s for $A = 0.9$.

Figure 8 shows the evolution of the bubble curvature ζ. Here, ζ is calculated using a least squares fit of a circle of radius $1/|\zeta|$ to all intersection points of the interface with the cell face within $|x|/\lambda \leq 0.12$. As predicted by non-local theoretical analysis, in the linear regime, the bubble curvature changes linear with time. Then, in the weakly non-linear regime, the curvature reaches an extremum followed by an asymptotic flattening of the bubble, i.e. a decrease in curvature for both values of A.

Finally, Figure 9 depicts the calculated bubble velocity v as a function of the absolute bubble curvature $|\zeta|$. Initially, the bubble exhibits an abrupt acceleration that is due to the interaction with the passing shock, whereas the curvature remains roughly unchanged. In the linear regime, the bubble curvature increases with only gradual changes in the bubble velocity. This result is consistent with linear theory, Eqs. (3.3)-(3.5). In

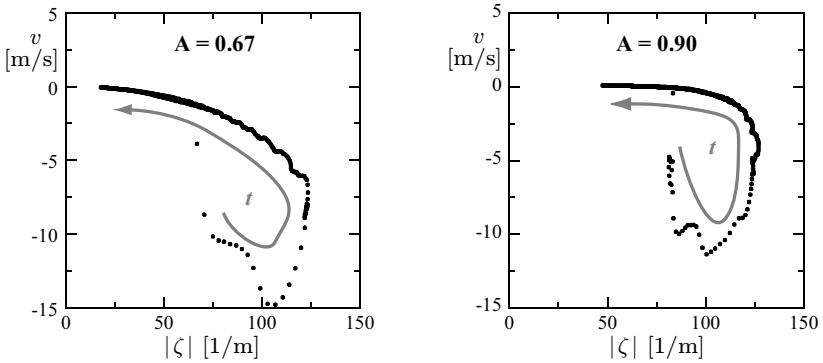

FIGURE 9. Bubble velocity v as function of absolute bubble curvature $|\zeta|$ for $A = 0.67$ (left) and $A = 0.9$ (right).

the weakly non-linear regime, the bubble velocity reaches a local maximum and then starts to decrease with almost constant curvature. Finally, the bubble curvature asymptotically tends to zero while the bubble continues to decelerate, as predicted by non-local theory. However, depending on the case, a slightly different bubble behavior is evident. For $A = 0.67$, the bubble both flattens and decelerates simultaneously. For $A = 0.9$, the bubble deceleration occurs prior to any significant decrease of ζ, thus leading to a flattening of the bubble front with only gradual changes in the bubble velocity.

In summary, these numerical results affirm the bubble behavior predicted by the non-local theory.

6. Conclusion

We performed systematic theoretical and numerical studies of the nonlinear large-scale coherent dynamics in the Richtmyer-Meshkov instability for fluids with contrast densities. Our simulations modeled the interface dynamics for compressible and viscous fluids. For a two-fluid system we observed that in the nonlinear regime of the instability the bubble velocity decays and its surface flattens, and the flattening is accompanied by slight oscillations. We found the theoretical solution for the system of conservation laws, describing the principal influence of the density ratio on the motion of the nonlinear bubble. The solution has no adjustable parameters, and shows that the flattening of the bubble front is a distinct property universal for all values of the density ratio. This property follows from the fact that the RM bubbles decelerate. The theoretical and numerical results validate each other, describe the new type of the bubble front evolution in RMI, and identify the bubble curvature as important and sensitive diagnostic parameter.

REFERENCES

ALON, U., HECHT, J., OFFER, D. & SHVARTS, D. 1995 Power laws and similarity of rayleigh-taylor and richtmyer-meshkov mixing fronts at all density ratios. *Phys. Rev. Lett.* **74**, 534–537.

BENJAMIN, R., BESNARD, D. & HAAS, J. 1993 Shock and reshock of an unstable interface. *Tech. Rep.* LANL Report No. LA-UR 92-1185. Los Alamos National Laboratory.

Bonazza, R. & Sturtevant, B. 1996 X-ray measurements of growth rates at a gas interface accelerated by shock waves. *Phys. Fluids* **8**, 2496–2512.

Chebotareva, E. I., Aleshin, A. N., Zaytsev, S. G. & Sergeev, S. V. 1999 Investigation of interaction between reflected shocks and growing perturbation on an interface. *Shock waves* **9** (2), 81–86.

Dimonte, G. 2000 Spanwise homogeneous buoyancy-drag model for rayleightaylor mixing and experimental evaluation. *Phys. Plasmas* **7**, 2255–2269.

Fedkiw, R., Aslam, T., Merriman, B. & Osher, S. 1999 A non-oscillatory Eulerian approach to interfaces in multimaterial flows (the ghost fluid method). *J. Comput. Phys.* **152**, 457–492.

Goncharov, V. N. 2002 Analytical model of nonlinear, single-mode, classical rayleigh-taylor instability at arbitrary atwood numbers. *Phys. Rev. Lett.* **88**.

Haan, S. W. 1991 Weakly nonlinear hydrodynamic instabilities in inertial fusion. *Phys. Fluids B* **3** (8), 2349–2355.

Holmes, R. L., Dimonte, G., Fryxell, B., Gittings, M. L., Grove, J. W., Schneider, M., Sharp, D. H., Velkovitch, A. L., Weaver, R. P. & Zhang, Q. 1999 Richtmyermeshkov instability growth: experiment, simulation and theory. *J. Fluid Mech.* **389**, 55–79.

Jacobs, J. & Sheeley, J. 1996 Experimental study of incompressible richtmyer-meshkov instability. *Phys. Fluids* **8**, 405–415.

Kull, F. 1991 *Physics Reports* .

LeVeque, R. 1990 *Numerical Methods for Conservation Laws*. Basel: Birkhäuser.

Matsuoka, C., Nishihara, K. & Fukuda, Y. 2003 Erratum: Nonlinear evolution of an interface in the richtmyer-meshkov instability [phys. rev. e 67, 036301 (2003)]. *Phys. Rev. E* **67** (029902), 1.

Meshkov, E. 1969 *Sov. Fluid Dyn.* **4**, 101.

Oron, D., Alon, U., Offer, D. & Shvarts, D. 2001 Dimensionality dependence of the rayleightaylor and richtmyermeshkov instability late-time scaling laws. *Phys. Plasmas* **8**, 2883–2889.

Osher, S. & Sethian, J. A. 1988 Fronts propagating with curvature-dependent speed: Algorithms based on Hamilton-Jacobi formulations. *J. Comput. Phys.* **79**, 12–49.

Pavlenko, A. V., Baishev, A. I., Kucherenko, Y. A., Litvin, A. T. & Sorokatyi, N. N. 2000 Experimental investigation into the interaction of the stationary shock wave with the turbulent layer. *Laser Part. Beams* **18** (2), 171–174.

Richtmyer, R. 1960 *Commun. Pure & Appl. Math.* **13**, 297.

Schneider, M., Dimonte, G. & Remington, B. 1998 Large and small scale structure in rayleigh-taylor mixing. *Phys. Rev. Lett.* **80**, 3507–3510.

Smiljanovski, V., Moser, V. & Klein, R. 1997 A capture-tracking hybrid scheme for deflagration discontinuities. *Combust. Theory Modelling* **1**, 183–215.

Strang, G. 1967 On the construction and comparison of difference schemes. *SIAM J. Num. Anal.* **5**, 506–517.

Vandenboomgaerde, M., Mugler, C. & Gauthier, S. 1998 Impulsive model for the richtmyer-meshkov instability. *Phys. Rev. E* **58**, 1874–1882.

Velikovich, A. & Dimonte, G. 1996 Nonlinear perturbation theory of the incompressible richtmyer-meshkov instability. *Phys. Rev. Lett.* **76**, 3112–3115.

Wouchuk, J. 2001 Growth rate of the linear richtmyer-meshkov instability when a shock is reflected. *Phys. Rev. E* **63** (056303), 1–13.